Published in final edited form as:

Am J Med Genet A. 2020 May ; 182(5): 1117–1129. doi:10.1002/ajmg.a.61532.

Brain morphological analysis in *PTEN* hamartoma tumor syndrome

Tadashi Shiohama[1,2], **Jacob Levman**[1,3], **Lana Vasung**[1], **Emi Takahashi**[1]

[1]Division of Newborn Medicine, Department of Medicine, Boston Children's Hospital, Harvard Medical School, Boston, Massachusetts

[2]Department of Pediatrics, Chiba University Hospital, Chiba, Japan

[3]Department of Mathematics, Statistics and Computer Science, St. Francis Xavier University, Antigonish, NS, Canada

Abstract

PTEN hamartoma tumor syndrome (PHTS) is a spectrum of hereditary cancer syndromes caused by germline mutations in *PTEN*. PHTS is of high interest, because of its high rate of neurological comorbidities including macrocephaly, autism spectrum disorder, and intellectual dysfunction. Since detailed brain morphology and connectivity of PHTS remain unclear, we quantitatively evaluated brain magnetic resonance imaging (MRI) in PHTS. Sixteen structural T1-weighted and 9 diffusion-weighted MR images from 12 PHTS patients and neurotypical controls were used for structural and high-angular resolution diffusion MRI (HARDI) tractography analyses. Mega-corpus callosum was observed in 75%, polymicrogyria in 33%, periventricular white matter lesions in 83%, and heterotopia in 17% of the PHTS participants. While gyrification index and hemispheric cortical thickness showed no significant differences between the two groups, significantly increased global and regional brain volumes, and regionally thicker cortices in PHTS participants were observed. HARDI tractography showed increased volume and length of callosal pathways, increased volume of the arcuate fasciculi (AF), and increased length of the bilateral inferior longitudinal fasciculi (ILF), bilateral inferior fronto-occipital fasciculi (IFOF), and bilateral uncinate fasciculus. A decrease in fractional anisotropy and an increased in apparent diffusion coefficient values of the AF, left ILF, and left IFOF in PHTS.

Keywords

HARDI; mega corpus callosum; megalencephaly; *PTEN* hamartoma tumor syndrome; structural brain MRI

Correspondence: Tadashi Shiohama, Department of Pediatrics, Chiba University Hospital, 1-8-1 Inohana, Chuo-ku, Chiba-shi, Chiba 260-8670, Japan. asuha_hare@yahoo.co.jp.

AUTHOR CONTRIBUTIONS

T.S. was responsible for study design. T.S., J.L and E.T. analyzed data of structural MRI and HARDI tractography, and T.S., J.L., L.V. and E.T. wrote/edited the manuscript.

CONFLICT OF INTEREST

T.S., J. L., L. V., and E. T. declare relevant no conflicts of interest.

SUPPORTING INFORMATION

Additional supporting information may be found online in the Supporting Information section at the end of this article.

1 | INTRODUCTION

The phosphatase and tensin homolog (PTEN) protein plays a pivotal role in growth, proliferation, and polarization in neurons mainly via negative regulation of the PI3K/AKT/mTOR signaling pathway (Leslie & Longy, 2016). *PTEN* hamartoma tumor syndrome (PHTS) is a spectrum of disorders caused by germline mutations in the *PTEN* gene. It is clinically divided into several syndromes including Cowden syndrome (OMIM 158350), Bannayan–Riley–Ruvalcaba syndrome (OMIM 153480), Macrocephaly/autism syndrome (OMIM 605309), and adult Lhermitte–Duclos syndrome (OMIM 158350) (Balci et al., 2018). PHTS syndromes are sometimes inaccurately classified during childhood mostly because clinical manifestations of these syndromes overlap, and cancers, which are essential for the correct clinical diagnosis of Cowden syndrome or Bannayan–Riley–Ruvalcaba syndrome usually occur after the later part of the third decade of life.

Although PHTS is recognized mainly as a hereditary cancer syndrome, numerous clinical case reports indicate a high rate of comorbidities such as macrocephaly (measured with head circumference) (43–100%) (Hansen-Kiss et al., 2017; Kato et al., 2018; Kurata et al., 2018), autism spectrum disorder (ASD) (14–50%) (Balci et al., 2018; Hansen-Kiss et al., 2017; Kato et al., 2018; Kurata et al., 2018), and intellectual dysfunction/developmental delay (31–67%) (Hansen-Kiss et al., 2017; Kato et al., 2018; Kurata et al., 2018).

While studies of brain morphology in PHTS are few and limited in qualitative analysis, typical findings such as posterior periventricular lesions with T2-weighted hyperintensities have been reported (Balci et al., 2018; Lok et al., 2005; Vanderver et al., 2014). However, to our knowledge, quantitative analysis of brain structure or fiber pathways using structural/diffusion-weighted MRI or diffusion MRI tractography have not yet been reported. In this study, we report quantitative measures of brain regions in patients with PHTS and controls, including regional volume, cortical thickness, and surface curvature, together with quantitative measures of fiber pathways.

2 | MATERIAL AND METHODS

2.1 | Subjects

This retrospective study was approved by the Institutional Review Board at Boston Children Hospital (BCH). We have reviewed electronic medical records of patients treated in BCH from June 1, 2008 to May 31, 2016 using i2b2 (http://web2.tch.harvard.edu/i2b2) to assemble our listing of patients with PHTS. Multiple images from the same subjects were scanned with at least 1-year interval, therefore, we assumed independence of these measures. The gender- and age-matched neurotypical controls (NC) were selected from our in-house database composed of electronic records of healthy participants without neurological disorders, neuropsychological disorders, or epilepsy (Levman, MacDonald, Lim, Forgeron, & Takahashi, 2017). Both datasets (neurotypical and PHTS) were comprised of examinations acquired at BCH. For this type of study formal consent is not required.

2.2 | Structural MRI acquisition and processing

All participants were imaged with clinical 3T MRI scanners (MAGNETOM Skyra, Siemens Medical Systems, Erlangen, Germany) at BCH. DICOM files of 3D T1-weighted MPRAGE (TR 2,000–2,520 ms; TE 1.7–2.6 ms, voxel size 0.52–1.0 × 0.52–1.0 × 0.9–1.0 mm, matrix 256 × 256) were accessed through the Children's Research and Integration System (Pienaar, Rannou, Bernal, Hahn, & Grant, 2015), and analyzed with CIVET version 2.1.0 pipeline (Zijdenbos, Forghani, & Evans, 2002) using CBRAIN platform (Sherif, Rioux, Rousseau, et al., 2014). The brain structural analysis using the CIVET pipeline included correction for intensity nonuniformity artifacts by the N3 algorithm (Sled, Zijdenbos, & Evans, 1998), nonlinear registration to a stereotaxic ICBM152 2009 template space (Fonov, Evans, McKinstry, Almli, & Collins, 2009), brain masking (Smith, 2002), tissue classification using an artificial neural network classifier (INSECT) (Tohka, Zijdenbos, & Evans, 2004; Zijdenbos et al., 2002), and brain segmentation using ANIMAL (Collins, Zijdenbos, Baaré, & Evans, 1999). The surface of gray matter (GM) and white matter (WM) were extracted with 40,962 vertices per hemisphere using the t-laplace metric (Kim et al., 2005), and triangular meshes between them were used to measure average cortical thickness, volume, gyrification index (GI), and cortical surface area in different brain regions in each hemisphere (Boucher, Whitesides, & Evans, 2009; Lerch & Evans, 2005). The quality of the outputs of the CIVET pipeline (shapes of the brain mask, linear/nonlinear registration to the template, tissue classification, and brain segmentation) were manually inspected for quality. This resulted in 16 volumetric structural brain MR images from 12 PHTS patients, after excluding cases with genetic variants of unknown significance, or without volumetric brain MRI. Gender and age at MRI scans were significantly matched to controls (ratio of males, PHTS 12/16, NC 12/16; age at scans, PHTS mean 10.6 years old [SD 5.6], NC 10.7 [5.8], [$T(30) = -0.02$, $p = .98$]).

2.3 | Diffusion MRI tractography

Thirty diffusion-weighted measurements ($b = 1{,}000$ s/mm^2) and 1–10 nondiffusion weighted measurements ($b = 0.22$ s/mm^2) were acquired with clinical 3 T MRI scanners (TR 5,504–11,000 ms; TE 88–94 ms; voxel size 1.64–2.0 × 1.64–2.0 × 2.0 mm; matrix size 128 × 128; flip angle 90° with a head coil). Images with motion artifacts were excluded based on visual assessment (motion correction software was not used). Diffusion MR images were obtained from nine participants (Cases 2–4, 6–10, and 12). High-angular resolution diffusion MR imaging (HARDI) (Tuch et al., 2002) was used to reconstruct pathways by using Diffusion Toolkit (http://trackvis.org), using a FACT algorithm with an angle threshold of 45°. We did not use an FA threshold to terminate tractography (e.g., Takahashi, Folkerth, Galaburda, & Grant, 2012), but instead used a brain mask to perform tractography within the brain. Callosal pathways (CP) and six associational cortico-cortical pathways (arcuate fasciculus [AF], inferior longitudinal fasciculus [ILF], inferior fronto-occipital fasciculus [IFOF], uncinate fasciculus [UF], cingulum fasciculus [CF], and fornix fasciculus ff) in the both hemispheres were identified and visualized using TrackVis (http://trackvis.org), as in previous analyses (Cohen et al., 2016; Takahashi et al., 2012; Xu et al., 2014).

Anatomic and tractography atlases (Catani & Thiebaut de Schotten, 2008; Mori & Tournier, 2013; Thiebaut de Schotten, Ffytche, et al., 2011) were used to guide regions of interest

(ROIs) placements on nondiffusion-weighted (b0) images and color FA maps in order to delineate the pathways of interest. A neuroscientist (E.T.) identified all tracts studied through manual ROI placement and assessed resulting courses of fiber pathways. For the CF and FF pathways, several ROIs were placed along the white matter regions for each pathway shown in the atlases. For the CP, an ROI was drawn in the corpus callosum in a median sagittal plane. For the ILF, IFOF, and UF pathways, two sphere ROIs were used for each pathway in their destinations: anterior temporal and occipital regions for the ILF, inferior frontal and occipital regions for the IFOF, and inferior frontal and anterior temporal regions for the UF. These ROIs were used as starting and stopping ROIs. When we did not identify any pathways between the starting/stopping ROIs, the distance between the two ROIs were gradually reduced until we find a part of the pathways (Figure 1a–d). Excess erroneous pathways due to the large size of the ROIs were manually excluded using additional sphere ROIs. The size of all the ROIs were carefully optimized to not include other white matter pathways, as well as not to miss the arcuate pathways, by changing the size and location several times.

The volume, length, fractional anisotropy (FA), and apparent diffusion coefficient (ADC) of each identified pathway were calculated and compared with NC participants. Gender and age at MRI scans were not statistically significantly different from our controls (ratio of males, PHTS 5/9, NC 5/9; age at scans, PHTS mean 7.2 years old [SD 4.3], NC 7.7 [4.1], [$T(16) = 0.26$, $p = .80$]).

2.4 | Statistical analysis

Each brain structure and fiber pathway measurement in PHTS and normal control participants were evaluated through Levene's test for equality of variances and two-tailed unpaired t tests with the Bonferroni correction for multiple comparisons. We determined $p < 5 \times 10^{-4}$ ($\alpha = .05$ for 100 repeating t tests) for the structural analyses as a statistical significance level. Univariate General Linear Model test ($p < .05$) was constructed to evaluate the effects of continuous or binary covariates (the presence of PHTS, age, and gender) on the measurements of the diffusion MRI analysis. Critical values from the F-distribution calculation were determined to be $F(0.05,4,13) = 3.18$ and $F(0.05,1,13) = 4.67$, for the corrected model and each covariate, respectively. IBM SPSS Statistics version 19 (IBM Corp. Armonk, NY) and PRISM 6 (Graph Pad software, CA) were used for the statistical analysis and graph visualization, respectively. For the cortical thickness analysis and visualization, we used SurfStat toolbox (http://www.math.mcgill.ca/keith/surfstat/) that runs on MATLAB R2016a (MathWorks, Natick, MA). Cortical thicknesses were visualized as t-statistics maps (Figure 2a) and random field theory (RFT) maps. A cluster level correction was used for the RFT maps, with a significance level of $p \leq .02$ (Figure 2b).

3 | RESULTS

3.1 | Patient characteristics

Clinical diagnoses in the PHTS patients included were Bannayan–Riley–Ruvalcaba syndrome in 33% (4/12), Macrocephaly/autism syndrome in 33% (4/12), and unclassified in 33% (4/12). 42% (5/12) of patients with PHTS had ASD, 92% (11/12) had macrocephaly

(head circumference above 95th centile), 42% (5/12) had lower intelligence quotient (IQ) (≤75), 25% (3/12) had mucocutaneous lesions, and 33% (4/12) had thyroid nodules (Table 1 and Table S1). Cancer was not reported in any of the included PHTS patients. The most common genetic variants, if present, were as follows: missense variants (six patients), variants in the promoter region (three patients), truncating variant (one patient), a large deletion (one patient), and a splice site variant (one patient).

3.2 | Qualitative analysis

Mega corpus callosum (CC) (Hengst, Tücke, Zerres, Blaum, & Häusler, 2010; Pierson, Zimmerman, Tennekoon, & Bönnemann, 2008) was present in 75% (9/12), polymicrogyria 33% (4/12) (Figure 3a, arrows), periventricular WM lesions with T2 hyperintensities in 83% (10/12), and periventricular heterotopia in 17% (2/12) of PHTS participants (Table 1, Table S1). The NC group showed no structural brain abnormalities (Figure 3e,f). The brains of PHTS patients were elongated in the anterior–posterior direction (Figure 3c,d), compared with NCs (both are 9.8 years old male) (Figure 3g,h).

3.3 | Global brain volumes

PHTS patients showed significantly larger volumes of cortical GM (The rate of PHTS/NC = 1.5, $T[17.07] = 5.18$, $p < .0001$), and of WM (The rate of PHTS/NC = 1.8, $T[22.67] = 6.35$, $p < .0001$) (Table 2). PHTS cases caused by a variant in the promoter region (Case 1, 2, 5 as shown on Table S1) showed a moderate increase of GM and WM despite their association with macrocephaly (Figure 4). A correlation between brain volumes and age in each group was not found (Figure 4).

3.4 | Global cortical surface area, gyrification, volume, and cortical thickness

The cortical surface analysis showed that PHTS patients have larger cortical surface area and volume of both hemispheres (Table 3), while the GI and average cortical thickness were not statistically significantly different between the PHTS and NC (Table 3).

3.5 | Regional volume and cortical thickness

The regional volumetric analysis showed significantly larger volume in all regions of GM and WM of the brain and brainstem and an increased volume of cerebellar hemispheres in PHTS patients compared to NC (Table 4).

Figure 2 and Figure S1 show a cortical thickness map superimposed on a 3-dimensional template brain surface image. The t-statistics for the differences between PHTS and NC groups showed increased thickness in the left dorsolateral frontal cortex, bilateral postcentral gyrus, left parietal lobe, right superior parietal lobule, bilateral orbitofrontal, and right occipito-temporal junction, and decreased thickness in the right lateral temporal lobe in PHTS (Figure 2a). Differences observed in the left dorsolateral frontal cortex, bilateral postcentral gyrus, left parietal lobe, and right superior parietal lobule were statistically significant at the cluster level using the RFT (Figure 2b). Decreased thickness in the right lateral temporal lobe in PHTS was not statistically significant using the RFT (not shown).

3.6 | HARDI tractography

The AF was not detected in Case 8, and the trajectory of the IFOF in Case 7 was clearly abnormal, coursing between the occipital and temporal lobes (Figure 1). Therefore, the measurements of the AF and IFOF were compared between eight participants in each group (Table 5), excluding the subjects with diffusion MR images of low quality. The volume and the length of the CP, and the length of the bilateral ILF, bilateral IFOF, and right UF were statistically significantly increased with large size effects (absolute Cohen's $d > 0.8$). The ratio of PHTS to NC in length ranged from 1.0 to 2.1, while the ratio in volume ranged from 0.6 to 1.9. FA and ADC values showed no statistically significant differences except for the statistically significantly increased ADC values of the left ILF.

Univariate General Linear Model test showed statistically significant changes (increased volume and length of the CP, and increased length of the IFOF, ILF, and UF in PHTS), independent of their age and gender (Table 5).

4 | DISCUSSION

We quantitatively evaluated brain morphology of PHTS patients using structural and diffusion-weighted brain MRI, and diffusion tractography. Our results show larger overall brain volume and cortical surface area in PHTS patients compared to NC. Regional analyses showed that all segmented brain regions had significantly increased volume in the PHTS patients, while more specific regions (left dorsolateral frontal cortex, bilateral postcentral gyrus, left parietal lobe, and right superior parietal lobule) showed increased cortical thickness. Diffusion MRI tractography analyses also identified several changes: the CP, bilateral ILF, bilateral IFOF, and right UF showed significant elongation, and the left ILF showed increased ADC values in patients with PHTS.

4.1 | Anatomical characteristics of PHTS brain

In addition to high periventricular T2 signal intensity and megalencephaly (increased brain size) as previously noted (Balci et al., 2018; Lok et al., 2005; Vanderver et al., 2014), our qualitative observation in MR images of patients with PHTS showed a more frequent occurrence of mega CC, perisylvian polymicrogyria, and periventricular heterotopia. The observation of the mega CC in PHTS was in agreement with our quantitative HARDI tractography findings in which CP of the PHTS patients were significantly increased in volume and length.

PHTS is one of the syndromes with constitutive hyperactivity of the PI3K/AKT/mTOR signaling pathway due to mutations of genes responsible for coding for proteins within the pathway. The hyperactivity of the PI3K/AKT/mTOR signaling pathway is one of the major causes of megalencephaly, and other origins of megalencephaly include Sotos syndrome (OMIM 117550), Gorlin syndrome (OMIM 109400), and Canavan disease (OMIM 271900), which need to be differentially diagnosed from PHTS. Patients with Sotos syndrome (Türkmen et al., 2015), Gorlin syndrome (Shiohama et al., 2017), and Canavan syndrome (Brismar, Brismar, Gascon, & Ozand, 1990), present with thinner CC, while in the current study, patients with PHTS showed increased volume and fiber pathways throughout the CC.

Hyperactivity of the PI3K/AKT/mTOR signaling pathway also leads to several megalencephaly and overgrowth syndromes, such as Megalencephaly-polymicrogyria-polydactyly-hydrocephalus syndrome (MPPH) (OMIM 603387, 615937, 615938) (Mirzaa et al., 2012), Megalencephaly-capillary malformation-polymicrogyria syndrome (MCAP) (OMIM 602501) (Mirzaa et al., 2012), and PIK3CA-related overgrowth spectrum (PROS) (Keppler-Noreuil et al., 2015). Both PHTS and MPPH/MCAP have common pathological activation in the PI3K/mTOR/AKT signaling pathway. In MPPH/MCAP, perisylvian polymicrogyria, megalencephaly, mega CC, cerebellar tonsillar ectopia are often observed, found in 86% (36/42), 100% (42/42), 17% (7/42), and 64% (27/42), respectively (Mirzaa et al., 2012). Given the thinner CC in Sotos syndrome, Gorlin syndrome, and Canavan syndrome, the mega CC may be a key finding of PHTS and MPPH/MCAP.

A key differential observation between PHTS and MPPH/MCAP is the presence of hydrocephalus or ventriculomegaly which is found in 76% (32/42) in MPPH/MCAP (Mirzaa et al., 2012). These comorbidities in MPPH/MCAP often suddenly worsen in the infantile period, and need emergent neurosurgery procedures. Interestingly, hydrocephalus or ventriculomegaly was not detected through radiological readings in patients with PHTS in the current study, and the enlargement of lateral ventricles was only found by the MRI volumetric analysis.

Given that clinical treatment is different between PHTS and MPPH/MCAP (i.e., autism spectrum syndrome in childhood and tumorigenesis in adulthood for PHTS, and progressive hydrocephalus for MPPH/MCAP), it is critical to accurately diagnose these cases. However, the genetic diagnosis for PHTS is sometimes challenging because PHTS is caused not only by *PTEN*-coding regional mutations, but also numerical abnormal karyotypes or promoter region mutations. Therefore, the presence of the enlargement of lateral ventricles and CC can be important biomarkers for differential diagnosis of PHTS and MPPH/MCAP. While malignancies in PTHS generally occur after their adult age, hydrocephalus and ventriculomegaly in MPPH/MCAP should be identified in the early infantile period. Therefore, neuroimaging in patients with macrocephaly should be conducted in the early infantile period.

4.2 | Cortical thickness, GI, and segmentation volume in PHTS brain

The quantitative study of structural brain MRI revealed that PHTS participants have significantly larger volumes in overall brain tissues including cortical GM, WM, cerebellar, and basal ganglia compared with NC participants.

The cortical folding has been hypothesized to be a result of the regional neuronal differentiation and migration (Zilles, Armstrong, Schleicher, & Kretschmann, 1988), and mechanical tension by the underlying axonal connections (Van Essen, 1997). More recent research revealed that an increased number of neural progenitors in the sub-ventricular zone are essential for gyrification of the cortical cortex (Matsumoto, Shinmyo, Ichikawa, & Kawasaki, 2017). The GI is an index representing the degree of gyrification; the ratio of the contour of the pial surface against the outer contour of the cerebral cortex, representing the degree of cortical folding (Matsuda & Ohi, 2018).

Within a species, increased total brain size has been positively correlated with larger cortical surface area (Harrison, Hof, & Wang, 2002; Hofman, 1985; Kazu, Maldonado, Mota, Manger, & Herculano-Houzel, 2014), increased number of neurons (Kazu et al., 2014), decreased GI (Rogers et al., 2010), and lower neuronal density (Harrison et al., 2002) in mammalian brains. Although the size of the normal human brain is negatively correlated with GI (Rogers et al., 2010), patients with PHTS in our study showed no difference in GI in spite of remarkably increased GM and WM volumes compared to that in NC. From these observations, one could speculate that, in normal brains, when the brain is relatively large, some mechanisms to decrease GI and the density of neurons are important to keep the brain neurologically healthy, while in the PHTS brain, such mechanisms likely associated with *PTEN* genes or the PI3K/AKT/mTOR pathway are not functioning appropriately which may result in a lack of statistically significant decreases in GI.

4.3 | Impairment of brain development by mutated PTEN

The pathological knowledge in the human brain with PHTS is very limited. In the cerebellum of Lhermitte–Duclos syndrome, the normal internal granule layer was replaced by an abnormal layer including hypertrophic ganglion cells, an abnormally myelinated molecular layer, and a thinner Purkinje cell layer (Abel et al., 2005; Rusiecki & Lach, 2016; Shiurba et al., 1988). Additionally, concerning the cerebrum, a single autopsy case of Lhermitte–Duclos syndrome showed meningeal nests of heterotopic, glio-neuronal and glial tissue in the gray matter, and increased telangiectatic capillaries in the white matter (Rusiecki & Lach, 2016).

The functions of the *PTEN* gene in the central nervous system have been mainly investigated with PTEN neuronal conditional knock-out mice by Cre-loxP system (Fraser, Bayazitov, Zakharenko, & Baker, 2008; Goebbels et al., 2010; Kwon et al., 2006; Maire et al., 2014). *PTEN c*onditional knockout mice have enlarged caliber of neuronal projections, increased dendritic spine density (Fraser et al., 2008), and increased glial cells, leading to hypermyelination (Goebbels et al., 2010; Maire et al., 2014). Subsequently, the transient hypermyelination is followed by the unraveling of the myelin sheath and severe myelination defects (Fraser et al., 2008). In addition, mutant Schwann cells can be triggered to myelinate unusual targets such as numerous axons <1 μm in diameter, spirally enwrap C-fiber axons in Remak bundles, and even collagen fibrils (Goebbels et al., 2010). This impairment of the central nervous system leads to a later onset leukodystrophy (Maire et al., 2014), macrocephaly (Kwon et al., 2006), and the behavioral deficiencies related to impaired social interaction, increased anxiety behavior, and memory-deficiency (Kwon et al., 2006).

4.4 | HARDI-derived fibers in PHTS

HARDI tractography in PHTS showed increased volume and length of the CP, increased volume of the AF, and increased length of the ILF, IFOF, and UF, independently of age or gender. To the best of our knowledge, only a few DTI studies have reported megalencephaly syndrome including PHTS. One reported FA and ADC values of the WM in patients with hemimegalencephaly (two early infants and one young adult) (Oikawa et al., 2015). Hemimagalencephaly is caused by a somatic mutation of some genes in the PI3K/AKT/mTOR pathway (Lee et al., 2012). Oikawa and colleagues reported increased

FA and decreased ADC in the subcortical WM of affected hemispheres of patients with hemimegalencephaly, and speculated that their results were due to excessive fiber bundles that caused increased axonal density and decreased free water in the extracellular space (Oikawa et al., 2015). Our HARDI results showed decrease FA values and increased ADC values of the AF, left ILF, and left IFOF in PHTS. These results indicate that it is possible that there are differential connectional abnormalities between hemimegalencephaly and PHTS, and the increase of axonal density in patients with PHTS may be milder than that in patients with hemimegalencephaly. In addition, four out of nine PHTS cases in our study accompanied polymicrogyria around the sylvian fissure. Prior DTI studies in polymicrogyria showed decreased FA and increased ADC through long association pathways and the CP (Andrade et al., 2015; Im, Paldino, Poduri, Sporns, & Grant, 2014). The presence of polymicrogyria in our PHTS cases may have contributed to the increased ADC in the left ILF.

We used a HARDI reconstruction for our diffusion MRI data. Although theoretically higher b values would benefit a HARDI reconstruction, we have experienced that a HARDI reconstruction in general gives us anatomically more accurate results. Tournier et al., certainly recommend that studies be conducted with a minimum of 45 angular diffusion directions as they said it “is sufficient to fully characterize the DW signal” (Tournier, Calamante, & Connelly, 2013). While they recommend the inclusion of 8 integer harmonic degrees (spherical harmonics) to characterize a diffusion weighted (DW) signal, they also point out if the recommended number of diffusion volumes could not be acquired due to the limitation of scan time, the eighth integer spherical harmonic degree is negligible, so in these situations we actually only need 28 DW directions (Tournier et al., 2013). Our study included 30, an additional 2 directions over the limited scan time recommendations (Tournier et al., 2013).

4.5 | Limitations

Our study did not include the assessment of neurocognitive functions in PHTS; therefore, it is difficult to directly connect the findings in structural MRIs with cognitive dysfunction in PHTS. Additionally, the possible presence of selection bias (healthcare access bias) could not be excluded, because our study is retrospective and performed at a single medical facility.

Most of genetic variations in PTEN in this study are pathogenic or likely pathogenic, but some cases dose not so. This study is for rare disease and carried in a single institution to keep uniformity in MRI acquisition. Therefore, we did not adopted a strict exclusion for enrolling patients in the view of genetic diagnosis.

Another limitation is that diffusion parameters in our study sometimes varied, although routine clinical scans usually use pre-set parameters to quickly diagnose. There are some sets of diffusion sequences with different numbers of high-b volumes (6, 12, 30, and 35 directions), but we chose data only with 35 directions and reported the number of $b = 0$ volumes. Unfortunately, bandwidth is not recorded in raw DICOM files so we are not able to obtain that information.

5 | CONCLUSION

We revealed detailed brain morphology in patients with PHTS using structural and diffusion MRI and HARDI tractography. Increased volume of multiple brain tissues and regions, regionally thicker cortex, and thin elongated IFOF and UF, were observed in PHTS. We think that understanding detailed brain morphology in megalencephalic syndromes will likely contribute to the improvement of differential diagnosis and lead to a better understanding how the responsible genes act in the central nerve system.

Supplementary Material

Refer to Web version on PubMed Central for supplementary material.

ACKNOWLEDGMENTS

This research project was supported by NIH R01HD078561, R21MH118739, R03NS101372 to E.T., JSPS KAKENHI Grant-in-Aid for Young Scientists (17K16241) to T.S., Natural Science and Engineering Research Council of Canada's Canada Research Chair grant (231266), a Canada Foundation for Innovation and Nova Scotia Research and Innovation Trust infrastructure grant (R0176004), and a St. Francis Xavier University research startup grant (R0168020) to J.L., and SNSF P300PB_167804 to L.V. We would like to thank Patrick MacDonald and Ashley Ruyan Lim for technical support.

DATA AVAILABILITY STATEMENT

The data that support the findings of this study are available from the corresponding author upon reasonable request.

Abbreviations:

ADC	apparent diffusion coefficient
AF	arcuate fasciculus
ASD	autism spectrum disorder
BCH	Boston Children Hospital
CC	corpus callosum
CF	cingulum fasciculus
CP	callosal pathways
DTI	diffusion tensor imaging
FA	fractional anisotropy
FF	fornix fasciculus
GI	gyrification index
GM	gray matter
HARDI	high-angular resolution diffusion MRI

IFOF	inferior fronto-occipital fasciculus
ILF	inferior longitudinal fasciculus
IQ	intelligence quotient
MCAP	megalencephaly-capillary malformation-polymicrogyria syndrome
MPPH	megalencephaly-polymicrogyria-polydactyly-hydrocephalus syndrome
MRI	magnetic resonance imaging
NC	neurotypical controls
PHTS	PTEN hamartoma tumor syndrome
PROS	PIK3CA-related overgrowth spectrum
PTEN	phosphatase and tensin homolog
RFT	random field theory
UF	uncinate fasciculus
WM	white matter

REFERENCES

Abel TW, Baker SJ, Fraser MM, Tihan T, Nelson JS, Yachnis AT, … Eberhart CG (2005). Lhermitte-Duclos disease: A report of 31 cases with immunohistochemical analysis of the PTEN/AKT/mTOR pathway. Journal of Neuropathology and Experimental Neurology, 64, 341–349. [PubMed: 15835270]

Andrade CS, Figueiredo KG, Valeriano C, Mendoza M, Valente KDR, Otaduy MCG, & Leite CC (2015). DTI-based tractography of the arcuate fasciculus in patients with polymicrogyria and language disorders. European Journal of Radiology, 84, 2280–2286. [PubMed: 26216794]

Balci TB, Davila J, Lewis D, Boafo A, Sell E, Richer J, … Sawyer SL (2018). Broad spectrum of neuropsychiatric phenotypes associated with white matter disease in PTEN hamartoma tumor syndrome. American Journal of Medical Genetics. Part B, Neuropsychiatric Genetics, 177, 101–109.

Boucher M, Whitesides S, & Evans A (2009). Depth potential function for folding pattern representation, registration, and analysis. Medical Image Analysis, 13, 203–214. [PubMed: 18996043]

Brismar J, Brismar G, Gascon G, & Ozand P (1990). Canavan disease: CT and MR imaging of the brain. American Journal of Neuroradiology, 11, 805–810. [PubMed: 2114773]

Catani M, & Thiebaut de Schotten M (2008). A diffusion tensor imaging tractography atlas for virtual in vivo dissections. Cortex, 44, 1105–113 [PubMed: 18619589]

2. Cohen AH, Wang R, Wilkinson M, MacDonald P, Lim AR, & Takahashi E (2016). Development of human white matter fiber pathways: From newborn to adult ages. International Journal of Developmental Neuroscience, 50, 26–38. [PubMed: 26948153]

Collins DL, Zijdenbos AP, Baaré WFC, & Evans AC (1999). ANIMAL+INSECT: Improved cortical structure segmentation. In Kuba A, Šáamal M, & Todd-Pokropek A (Eds.), Information processing in medical imaging. Lecture notes in computer science (Vol. 1613, pp. 210–223). Berlin, Heidelberg: Springer.

Fonov VS, Evans AC, McKinstry RC, Almli CR, & Collins DL (2009). Unbiased nonlinear average age-appropriate brain templates from birth to adulthood. NeuroImage, 47(Suppl 1), S102.

Fraser MM, Bayazitov IT, Zakharenko SS, & Baker SJ (2008). Phosphatase and tensin homolog, deleted on chromosome 10 deficiency in brain causes defects in synaptic structure, transmission and plasticity, and myelination abnormalities. Neuroscience, 151, 476–488. [PubMed: 18082964]

Goebbels S, Oltrogge JH, Kemper R, Heilmann I, Bormuth I, Wolfer S, … Nave KA (2010). Elevated phosphatidylinositol 3,4,5-trisphosphate in glia triggers cell-autonomous membrane wrapping and myelination. The Journal of Neuroscience, 30, 8953–8964. [PubMed: 20592216]

Hansen-Kiss E, Beinkampen S, Adler B, Frazier T, Prior T, Erdman S, … Herman G (2017). A retrospective chart review of the features of PTEN hamartoma tumor syndrome in children. Journal of Medical Genetics, 54, 471–478. [PubMed: 28526761]

Harrison KH, Hof PR, & Wang SS (2002). Scaling laws in the mammalian neocortex: Does form provide clues to function? Journal of Neurocytology, 31, 289–298. [PubMed: 12815248]

Hengst M, Tücke J, Zerres K, Blaum M, & Häusler M (2010). Megalencephaly, mega corpus callosum, and complete lack of motor development: Delineation of a rare syndrome. American Journal of Medical Genetics. Part A, 152A, 2360–2364. [PubMed: 20803648]

Hofman MA (1985). Size and shape of the cerebral cortex in mammals. I. the cortical surface. Brain, Behavior and Evolution, 27, 28–40.

Im K, Paldino MJ, Poduri A, Sporns O, & Grant PE (2014). Altered white matter connectivity and network organization in polymicrogyria revealed by individual gyral topology-based analysis. NeuroImage, 86, 182–193. [PubMed: 23954485]

Kato K, Mizuno S, Inaba M, Fukumura S, Kurahashi N, Maruyama K, … Saitoh S (2018). Distinctive facies, macrocephaly, and developmental delay are signs of a PTEN mutation in childhood. Brain & Development, 40, 678–684. [PubMed: 29752200]

Kazu RS, Maldonado J, Mota B, Manger PR, & Herculano-Houzel S (2014). Cellular scaling rules for the brain of Artiodactyla include a highly folded cortex with few neurons. Frontiers in Neuroanatomy, 8, 128. [PubMed: 25429261]

Keppler-Noreuil KM, Rios JJ, Parker VE, Semple RK, Lindhurst MJ, Sapp JC, … Biesecker LG (2015). PIK3CA-related overgrowth spectrum (PROS): Diagnostic and testing eligibility criteria, differential diagnosis, and evaluation. American Journal of Medical Genetics. Part A, 167A, 287–295. [PubMed: 25557259]

Kim JS, Singh V, Lee JK, Lerch J, Ad-Dab'bagh Y, MacDonald D, … Evans AC (2005). Automated 3-D extraction and evaluation of the inner and outer cortical surfaces using a Laplacian map and partial volume effect classification. NeuroImage, 27, 210–221. [PubMed: 15896981]

Kurata H, Shirai K, Saito Y, Okazaki T, Ohno K, Oguri M, … Maegaki Y (2018). Neurodevelopmental disorders in children with macrocephaly: A prevalence study and PTEN gene analysis. Brain & Development, 40, 36–41. [PubMed: 28774669]

Kwon CH, Luikart BW, Powell CM, Zhou J, Matheny SA, Zhang W, … Parada LF (2006). Pten regulates neuronal arborization and social interaction in mice. Neuron, 50, 377–388. [PubMed: 16675393]

Lee JH, Huynh M, Silhavy JL, Kim S, Dixon-Salazar T, Heiberg A, … Gleeson JG (2012). De novo somatic mutations in components of the PI3K-AKT3-mTOR pathway cause hemimegalencephaly. Nature Genetics, 44, 941–945. [PubMed: 22729223]

Lerch JP, & Evans AC (2005). Cortical thickness analysis examined through power analysis and a population simulation. NeuroImage, 24, 163–173. [PubMed: 15588607]

Leslie NR, & Longy M (2016). Inherited PTEN mutations and the prediction of phenotype. Seminars in Cell & Developmental Biology, 52, 30–38. [PubMed: 26827793]

Levman J, MacDonald P, Lim AR, Forgeron C, & Takahashi E (2017). A pediatric structural MRI analysis of healthy brain development from newborns to young adults. Human Brain Mapping, 38, 5931–5942. [PubMed: 28898497]

Lok C, Viseux V, Avril MF, Richard MA, Gondry-Jouet C, Deramond H, … Cancerology Group of the French Society of Dermatology. (2005). Brain magnetic resonance imaging in patients with Cowden syndrome. Medicine (Baltimore), 84, 129–136. [PubMed: 15758842]

Maire CL, Ramkissoon S, Hayashi M, Haidar S, Ramkissoon L, DiTomaso E, & Ligon KL (2014). Pten loss in Olig2 expressing neural progenitor cells and oligodendrocytes leads to interneuron dysplasia and leukodystrophy. Stem Cells, 32, 313–326. [PubMed: 24395742]

Matsuda Y, & Ohi K (2018). Cortical gyrification in schizophrenia: Current perspectives. Neuropsychiatric Disease and Treatment, 14, 1861–1869. [PubMed: 30050300]

Matsumoto N, Shinmyo Y, Ichikawa Y, & Kawasaki H (2017). Gyrification of the cerebral cortex requires FGF signaling in the mammalian brain. eLife, 14, 6.

Mirzaa GM, Conway RL, Gripp KW, Lerman-Sagie T, Siegel DH, deVries LS, … Dobyns WB (2012). Megalencephaly-capillary malformation (MCAP) and megalencephaly-polydactyly-polymicrogyria-hydrocephalus (MPPH) syndromes: Two closely related disorders of brain overgrowth and abnormal brain and body morphogenesis. American Journal of Medical Genetics. Part A, 158A, 269–291. [PubMed: 22228622]

Mori S, & Tournier JD (2013). Introduction to diffusion tensor imaging (1st ed., p. 140). California: Academic Press.

Oikawa T, Tatewaki Y, Murata T, Kato Y, Mugikura S, Takase K, & Takahashi S (2015). Utility of diffusion tensor imaging parameters for diagnosis of hemimegalencephaly. The Neuroradiology Journal, 28, 628–633. [PubMed: 26481187]

Pienaar R, Rannou N, Bernal J, Hahn D, & Grant PE (2015). ChRIS—A web-based neuroimaging and informatics system for collecting, organizing, processing, visualizing and sharing of medical data. Conference Proceedings: Annual International Conference of the IEEE Engineering in Medicine and Biology Society, 2015, 206–209.

Pierson TM, Zimmerman RA, Tennekoon GI, & Bönnemann CG (2008). Mega-corpus callosum, polymicrogyria, and psychomotor retardation: Confirmation of a syndromic entity. Neuropediatrics, 39, 123–127. [PubMed: 18671190]

Rogers J, Kochunov P, Zilles K, Shelledy W, Lancaster J, Thompson P, … Glahn DC (2010). On the genetic architecture of cortical folding and brain volume in primates. NeuroImage, 53, 1103–1108. [PubMed: 20176115]

Rusiecki D, & Lach B (2016). Lhermitte-Duclos disease with neurofibrillary tangles in heterotopic cerebral grey matter. Folia Neuropathologica, 54, 190–196. [PubMed: 27543776]

Sherif T, Rioux P, Rousseau ME, Kassis N, Beck N, Adalat R, … Evans AC (2014). CBRAIN: A web-based, distributed computing platform for collaborative neuroimaging research. Frontiers in Neuroinformatics, 8, 54. [PubMed: 24904400]

Shiohama T, Fujii K, Miyashita T, Mizuochi H, Uchikawa H, & Shimojo N (2017). Brain morphology in children with nevoid basal cell carcinoma syndrome. American Journal of Medical Genetics. Part A, 173, 946–952. [PubMed: 28328116]

Shiurba RA, Gessaga EC, Eng LF, Sternberger LA, Sternberger NH, & Urich H (1988). Lhermitte-Duclos disease. An immunohistochemical study of the cerebellar cortex. Acta Neuropathologica, 75, 474–480. [PubMed: 3287833]

Sled JG, Zijdenbos AP, & Evans AC (1998). A nonparametric method for automatic correction of intensity nonuniformity in MRI data. IEEE Transactions on Medical Imaging, 17, 87–97. [PubMed: 9617910]

Smith SM (2002). Fast robust automated brain extraction. Human Brain Mapping, 17, 143–155. [PubMed: 12391568]

Takahashi E, Folkerth RD, Galaburda AM, & Grant PE (2012). Emerging cerebral connectivity in the human fetal brain: An MR tractography study. Cerebral Cortex, 22, 455–464. [PubMed: 21670100]

Thiebaut de Schotten M, Ffytche DH, Bizzi A, Dell'Acqua F, Allin M, Walshe M, … Catani M (2011). Atlasing location, asymmetry and inter-subject variability of white matter tracts in the human brain with MR diffusion tractography. NeuroImage, 54, 49–59. [PubMed: 20682348]

Tohka J, Zijdenbos A, & Evans A (2004). Fast and robust parameter estimation for statistical partial volume models in brain MRI. NeuroImage, 23, 84–97. [PubMed: 15325355]

Tournier JD, Calamante F, & Connelly A (2013). Determination of the appropriate b value and number of gradient directions for high-angular-resolution diffusion-weighted imaging. NMR in Biomedicine, 26, 1775–1786. [PubMed: 24038308]

Tuch DS, Reese TG, Wiegell MR, Makris N, Belliveau JW, & Wedeen VJ (2002). High angular resolution diffusion imaging reveals intravoxel white matter fiber heterogeneity. Magnetic Resonance in Medicine, 48, 577–582. [PubMed: 12353272]

Türkmen S, Şahin S, Koçer N, Peters H, Mundlos S, & Tüysüz B (2015). Neuroimaging and clinical characterization of Sotos syndrome. Genetic Counseling, 26, 1–12. [PubMed: 26043501]

Van Essen DC (1997). A tension-based theory of morphogenesis and compact wiring in the central nervous system. Nature, 385, 313–318. [PubMed: 9002514]

Vanderver A, Tonduti D, Kahn I, Schmidt J, Medne L, Vento J, … van der Knaap M (2014). Characteristic brain magnetic resonance imaging pattern in patients with macrocephaly and PTEN mutations. American Journal of Medical Genetics. Part A, 164A, 627–633. [PubMed: 24375884]

Xu G, Takahashi E, Folkerth RD, Haynes RL, Volpe JJ, Grant PE, & Kinney HC (2014). Radial coherence of diffusion tractography in the cerebral white matter of the human fetus: Neuro-anatomic insights. Cerebral Cortex, 24, 579–592. [PubMed: 23131806]

Zijdenbos AP, Forghani R, & Evans AC (2002). Automatic ““pipeline”” analysis of 3-D MRI data for clinical trials: Application to multiple sclerosis. IEEE Transactions on Medical Imaging, 21, 1280–1291. [PubMed: 12585710]

Zilles K, Armstrong E, Schleicher A, & Kretschmann HJ (1988). The human pattern of gyrification in the cerebral cortex. Anatomy and Embryology (Berlin), 179, 173–179.

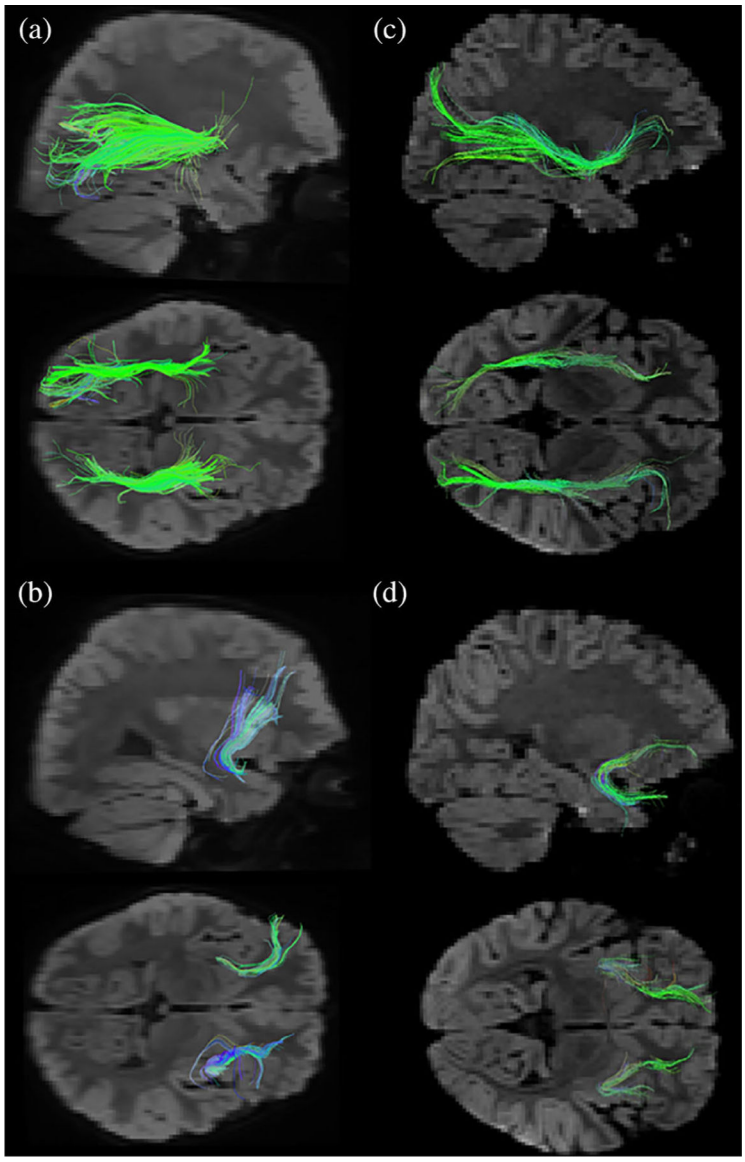

FIGURE 1.

High-angular resolution diffusion MR imaging tractography of PHTS Case 7 at 2.7 years old showing a fiber direction from left occipital to left insula with mimicking pathway of inferior fronto-occipital fasciculus (IFOF) (a), and right arcuate fasciculus (AF) with inadequate curvature projecting from temporal to the superior frontal (b). The tractography in the healthy female at 2.5 years old showing normal pathways of IFOF (c) and AF (d)

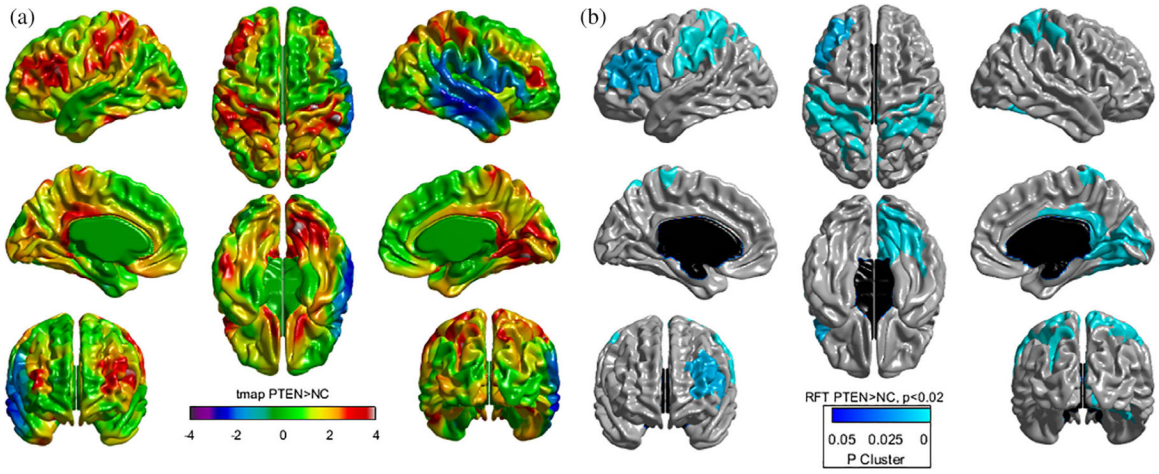

FIGURE 2.

Visualized cortical thickness with t-statistical map (tmap) (a), and random field theory (RFT) map (b, $p < .02$) showing thicker lesions in *PTEN* hamartoma tumor syndrome (PHTS, $N = 16$) than neurotypical controls (NC, $N = 16$). (a) In the color scale, blue and red indicate less and greater in mean cortical thickness in *PTEN* hamartoma tumor syndrome (PHTS), respectively, compared to that in the controls. (b) Blue indicates regions where patients with PHTS had significantly thicker cortex at the cluster level compared to the NC

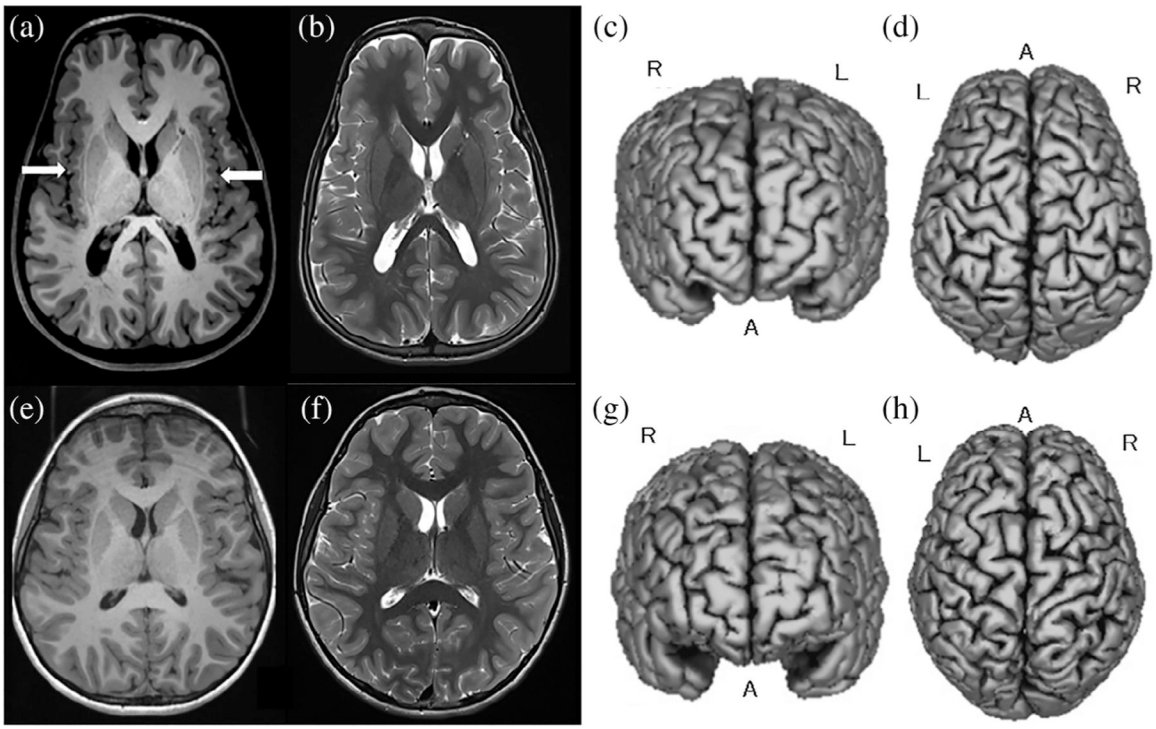

FIGURE 3.

T1-weighted images (a, e), T2-weighted images (b, f), and gray matter surfaces (c, d, g, h) in PHTS Case 9 (a–d) and normal 9.8 years old male control (e–h). The PHTS case showed frontal lobe bossing (a, b, d), bilateral perisylvian polymicrogyria (a, arrow)

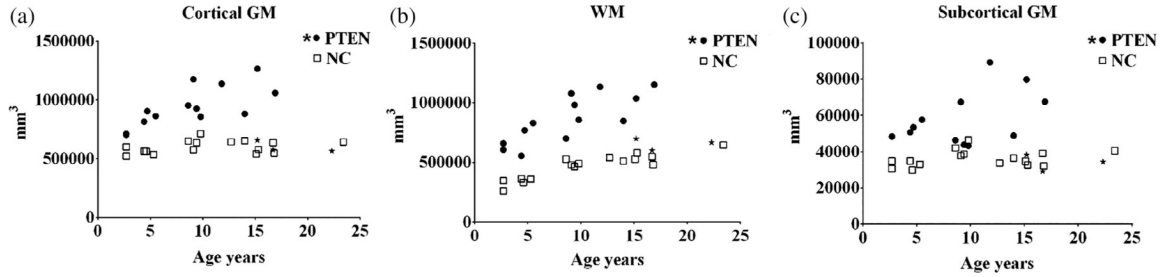

FIGURE 4.

The scatter plot between age and volumes of cortical gray matter (a), white matter (b), and subcortical gray matter (c) of *PTEN* hamartoma tumor syndrome (PHTS) (closed circle and asterisk) and normal controls (NC) (open square). The asterisk indicates PHTS due to variants of promoter regions

TABLE 1

The background of PHTS and NC participants

Category	PHTS (*N* = 16)	NC (*N* = 16)
Age of years (mean [SD]) *	10.6 [5.6]	10.7 [5.8]
Gender, ratio of male (% [*N*])	75% [12/16]	75% [12/16]
Clinical diagnosis (% [*N*])	BBRC 33% [4/12], MA 33% [4/12], unclassified 33% [4/12]	
ASD (% [*N*])	42% [5/12]	0% [0/16]
Macrocephaly ≥95th centile	92% [11/12]	0% [0/16]
IQ ≤75 (% [*N*])	42% [5/12]	0% [0/16]
Epilepsy (% [*N*])	17% [2/12]	0% [0/16]
Cancer (% [*N*])	0% [0/12]	0% [0/16]
Mucocutaneous lesions (% [*N*])	25% [3/12]	0% [0/16]
Thyroid nodules (% [*N*])	33% [4/12]	0% [0/16]
MRI abnormal findings (% [*N*])	Mega CC 75% [9/12], PMG 33% [4/12], PWML 83% [10/12], HT 17% [2/12]	0% [0/16]

Abbreviations: ASD, autism spectrum disorder; BBRC, Bannayan–Riley–Ruvalcaba syndrome; CC, corpus callosum; HT, heterotopia; IQ, intelligence quality; MA, macrocephaly/autism syndrome; NC, neurotypical controls; PHTS, *PTEN* hamartoma tumor syndrome; PMG, polymicrogyria; PWML, periventricular white matter lesions.

* $p = .98$ (two-tailed unpaired *t* analysis).

TABLE 2

The brain volume of PHTS and NC participants

Measurement	PHTS (*N* = 16) mean [SD]	NC (*N* = 16) mean [SD]	The rate of PHTS/NC	Cohen's *d*
CSF (mm^3)	61,109 [23395]	36,060 [12201]	1.7	1.34
Cortical GM (mm^3) *	878,791 [207352]	601,329 [54637]	1.5	1.83
WM (mm^3) *	823,261 [198981]	466,405 [104338]	1.8	2.25
Subcortical GM (mm^3)	52,896 [16090]	36,075 [4400]	1.5	1.43
Cortical GM/WM	1.08 [0.17]	1.35 [0.29]	0.8	−1.14

Abbreviations: CSF, cerebrospinal fluid; GM, gray matter; NC, neurotypical controls; PHTS, *PTEN* hamartoma tumor syndrome; SD, standard deviation; WM, white matter.

* $p < .0005$ (two-tail unpaired *t* test).

TABLE 3

The cortical surface of PHTS and NC participants

Measurement	PHTS (*N* = 16) mean [SD]	NC (*N* = 16) mean [SD]	The rate of PHTS/NC	Cohen's *d*
Gyrification index	3.81 [0.21]	3.76 [0.19]	1.0	0.25
L gyrification index	2.72 [0.15]	2.74 [0.14]	1.0	−0.14
R gyrification index	2.73 [0.16]	2.77 [0.15]	1.0	−0.26
L cortex surface area (mm^2) *	142,586 [23110]	103,455 [11776]	1.4	2.13
R cortex surface area (mm^2) *	142,499 [23186]	103,780 [12477]	1.4	2.08
L cortex average thickness (mm)	3.07 [0.32]	2.85 [0.23]	1.1	0.79
R cortex average thickness (mm)	2.95 [0.23]	2.86 [0.24]	1.0	0.38
L cortex volume (mm^3) *	419,593 [100696]	284,323 [31568]	1.5	1.81
R cortex volume (mm^3) *	415,352 [98141]	283,935 [30138]	1.5	1.81

Abbreviations: L, left hemisphere; NC, neurotypical controls; PHTS, *PTEN* hamartoma tumor syndrome; R, right hemisphere; SD, standard deviation.

* $p < .0005$ (two-tailed unpaired *t* test).

TABLE 4

The brain segmental volumes of PHTS and NC participants

Regions	PHTS (N = 16) mean [SD] (mm^3)	NC (N = 16) mean [SD] (mm^3)	The rate of PHTS/NC	Cohen's d
L frontal GM *	224,188 [51228]	152,677 [14853]	1.5	1.90
R frontal GM *	224,635 [51580]	153,147 [15525]	1.5	1.88
L frontal WM *	172,724 [42535]	94,893 [22224]	1.8	2.30
R frontal WM *	171,055 [48324]	94,766 [21551]	1.8	2.04
L temporal GM *	146,811 [33524]	100,973 [9127]	1.5	1.87
R temporal GM *	150,217 [33053]	102,772 [9954]	1.5	1.94
R temporal WM *	89,378 [22844]	50,182 [11670]	1.8	2.16
L temporal WM *	88,367 [22001]	50,262 [10941]	1.8	2.19
L parietal GM *	119,193 [26906]	78,048 [8083]	1.5	2.07
R parietal GM *	116,213 [22693]	77,470 [8295]	1.5	2.27
L parietal WM *	95,691 [24341]	52,213 [10512]	1.8	2.32
R parietal WM *	93,707 [19485]	52,000 [10434]	1.8	2.67
L occipital GM *	59,739 [11875]	40,121 [2469]	1.5	2.29
R occipital GM *	62,060 [16855]	40,136 [2827]	1.5	1.81
L occipital WM *	40,882 [12110]	24,989 [5068]	1.6	1.71
R occipital WM *	41,521 [9556]	25,469 [5922]	1.6	2.02
L thalamus *	10,737 [1716]	7,432 [982]	1.4	2.36
R thalamus *	10,746 [1696]	7,435 [993]	1.4	2.38
L caudate *	7,281 [1374]	4,572 [586]	1.6	2.57
R caudate *	6,967 [1133]	4,532 [559]	1.5	2.73
L fornix *	912 [149]	679 [144]	1.3	1.59
R fornix *	889 [144]	663 [142]	1.3	1.58
L globus pallidus *	1,533 [204]	1,085 [93]	1.4	2.83
R globus pallidus *	1,508 [214]	1,042 [97]	1.4	2.81

Regions	PHTS (*N* = 16) mean [SD] (mm^3)	NC (*N* = 16) mean [SD] (mm^3)	The rate of PHTS/NC	Cohen's *d*
L putamen *	6,312 [1089]	4,668 [493]	1.4	1.94
R putamen *	6,491 [1218]	4,747 [493]	1.4	1.88
L subthalamic nucleus *	76.4 [15.4]	54.1 [12.6]	1.4	1.59
R subthalamic nucleus *	78.1 [19.3]	53.5 [10.2]	1.5	1.59
Brainstem *	44,879 [12807]	30,191 [6386]	1.5	1.45
L cerebellum *	93,643 [14671]	71,268 [8632]	1.3	1.86
R cerebellum *	93,160 [14253]	71,563 [9119]	1.3	1.81
L lateral ventricle	9,252 [7632]	4,154 [2484]	2.2	0.90
R lateral ventricle	9,156 [6594]	3,912 [2102]	2.3	1.07
Third ventricle	2,263 [1395]	1,223 [749]	1.9	0.93
Fourth ventricle	2077 [792]	2,244 [1116]	0.9	−0.17
Extracerebral CSF	564,019 [141386]	392,396 [100012]	1.4	1.40

Abbreviations: CSF, cerebrospinal fluid; GM, gray matter; L, left; NC, neurotypical controls; PHTS, *PTEN* hamartoma tumor syndrome; R, right; SD, standard deviation; WM, white matter.

* $p < .0005$ (two-tailed unpaired *t* test).

Am J Med Genet A. Author manuscript; available in PMC 2021 August 14.

TABLE 5

The effect of covariates on HARDI tractography measurements in PHTS and NC; Univariate General Linear Model

Measurement	PHTS (*N* = 9) mean [SD]	NC (*N* = 9) mean [SD]	The rate of PHTS/NC	*R* squired	Corrected model	The presence of PHTS	Age	Gender
Volume (ml)								
AF, left	21.2 [13.5]	11.8 [6.4]	1.8	0.641	**F = 4.92** **$p = 0.016$**	**F = 14.2** **$p = 3.1 \times 10^{-3}$**	$F < 1.0 \times 10^{-4}$ $p = 0.99$	F = 3.58 $p = 0.085$
AF, right	19.1 [9.7]	11.5 [6.2]	1.7	0.602	**F = 4.16** **$p = 0.027$**	**F = 12.7** **$p = 4.5 \times 10^{-3}$**	F = 0.011 $p = 0.92$	F = 3.41 $p = 0.092$
ILF, left	18 [7.5]	9.5 [2.8]	1.9	0.667	**F = 5.51** **$p = 0.011$**	**F = 21.0** **$p = 7.8 \times 10^{-4}$**	F = 0.85 $p = 0.38$	F = 1.44 $p = 0.26$
ILF, right	13.6 [7.2]	9.0 [2.4]	1.5	0.409	F = 1.90 $p = 0.18$	F = 3.19 $p = 0.10$	F = 0.34 $p = 0.57$	F = 0.34 $p = 0.57$
IFOF, left	9.7 [7.9]	15.1 [3.8]	0.6	0.271	F = 1.02 $p = 0.44$	F = 1.7 $p = 0.22$	F = 0.14 $p = 0.71$	F = 0.79 $p = 0.39$
IFOF, right	12 [5.7]	17.0 [5.8]	0.7	0.184	F = 0.62 $p = 0.66$	F = 0.79 $p = 0.39$	F = 1.28 $p = 0.28$	F = 0.14 $p = 0.71$
UF, left	5 [3.4]	7.8 [2.2]	0.6	0.620	**F = 4.49** **$p = 0.022$**	F = 0.70 $p = 0.42$	F = 3.19 $p = 0.10$	F = 3.76 $p = 0.079$
UF, right	7.2 [3.7]	7.5 [2.1]	1.0	0.539	F = 3.22 $p = 0.056$	F = 1.65 $p = 0.23$	F = 0.78 $p = 0.40$	F = 3.35 $p = 0.094$
CF, left	10.7 [5.2]	7.1 [2.1]	1.5	0.730	**F = 7.43** **$p = 3.8 \times 10^{-3}$**	F = 2.95 $p = 0.11$	F = 1.21 $p = 0.29$	**F = 6.91** **$p = 0.023$**
CF, right	9.5 [5.4]	6.3 [1.4]	1.5	0.593	**F = 4.01** **$p = 0.03$**	F = 4.50 $p = 0.057$	F = 2.68 $p = 0.13$	F = 0.54 $p = 0.48$
FF, left	3.7 [2.1]	6.5 [1.9]	0.6	0.379	F = 1.68 $p = 0.22$	F = 2.50 $p = 0.14$	F = 0.14 $p = 0.72$	F = 0.001 $p = 0.98$
FF, right	4.3 [2.6]	6.8 [2.1]	0.6	0.297	F = 1.16 $p = 0.38$	F = 1.51 $p = 0.24$	F = 0.13 $p = 0.72$	F = 0.084 $p = 0.78$
CP	161.6 [31.2]	101.7 [23.9]	1.6	0.796	**F = 10.7** **$p = 8.7 \times 10^{-4}$**	**F = 38.9** **$p = 6.4 \times 10^{-5}$**	F = 4.26 $p = 0.063$	F = 4.28 $p = 0.063$
Lengths (mm)								
AF, left	57.4 [20.6]	49.2 [17.2]	1.2	0.500	F = 2.76 $p = 0.082$	F = 0.90 $p = 0.36$	F = 3.76 $p = 0.079$	F = 0.58 $p = 0.46$

Measurement	PHTS (*N* = 9) mean [SD]	NC (*N* = 9) mean [SD]	The rate of PHTS/NC	*R* squired	Corrected model	The presence of PHTS	Age	Gender
AF, right	47.5 [13.7]	46.1 [15.4]	1.0	0.226	F = 0.80 *p* = 0.55	F = 0.082 *p* = 0.78	F = 0.24 *p* = 0.63	F = 0.41 *p* = 0.54
ILF, left	81.7 [13.8]	48.6 [7.5]	1.7	0.777	**F = 9.58** ***p* = 1.4 × 10^{-3}**	**F = 36.7** ***p* = 8.2 × 10^{-5}**	F = 0.42 *p* = 0.53	F = 0.83 *p* = 0.38
ILF, right	74.5 [18.0]	43.5 [4.6]	1.7	0.884	**F = 21.0** ***p* = 4.1 × 10^{-5}**	**F = 62.9** ***p* = 7.1 × 10^{-6}**	F = 0.78 *p* = 0.40	F = 2.71 *p* = 0.13
IFOF, left	135.4 [19.7]	63.6 [12.5]	2.1	0.857	**F = 16.5** ***p* = 1.3 × 10^{-4}**	**F = 51.7** ***p* = 1.8 × 10^{-5}**	F = 0.041 *p* = 0.84	F = 1.58 *p* = 0.24
IFOF, right	132.5 [18.0]	66.3 [12.5]	2.0	0.891	**F = 22.6** ***p* = 3.0 × 10^{-5}**	**F = 89.6** ***p* = 1.3 × 10^{-6}**	F = 0.031 *p* = 0.86	F = 1.61 *p* = 0.23
UF, left	66.4 [19.5]	34.4 [5.9]	1.9	0.707	**F = 6.65** ***p* = 5.7 × 10^{-3}**	**F = 20.0** ***p* = 9.5 × 10^{-4}**	F = 1.01 *p* = 0.34	F = 2.24 *p* = 0.16
UF, right	89.2 [16.2]	40.1 [8.6]	2.2	0.917	**F = 30.6** ***p* = 6.6 × 10^{-6}**	**F = 107.9** ***p* = 5.1 × 10^{-7}**	F = 6.2 × 10^{-3} *p* = 0.94	F = 0.30 *p* = 0.60
CF, left	58.3 [28.4]	39.6 [8.2]	1.5	0.482	F = 2.56 *p* = 0.098	**F = 8.54** ***p* = 0.014**	F = 0.88 *p* = 0.37	F = 0.42 *p* = 0.53
CF, right	52.9 [24.8]	38.5 [11.9]	1.4	0.392	F = 1.77 *p* = 0.20	F = 2.67 *p* = 0.13	F = 0.023 *p* = 0.88	F = 2.20 *p* = 0.17
FF, left	54.2 [24.1]	44.5 [18.2]	1.2	0.124	F = 0.39 *p* = 0.81	F = 1.41 *p* = 0.26	F = 0.03 *p* = 0.87	F = 0.084 *p* = 0.78
FF right	53.5 [21.0]	42.0 [13.3]	1.3	0.397	F = 1.81 *p* = 0.20	F = 4.32 *p* = 0.062	F = 0.97 *p* = 0.35	F = 0.59 *p* = 0.46
CP	90.4 [7.8]	70.0 [10.6]	1.3	0.681	**F = 5.87** ***p* = 8.9 × 10^{-3}**	**F = 22.5** ***p* = 6.1 × 10^{-4}**	F = 0.48 *p* = 0.50	F = 0.43 *p* = 0.52
FA								
AF, left	0.42 [0.06]	0.47 [0.05]	0.9	0.698	**F = 6.36** ***p* = 6.7 × 10^{-3}**	**F = 8.62** ***p* = 0.014**	**F = 13.8** ***p* = 3.4 × 10^{-3}**	F = 0.18 *p* = 0.68
AF, right	0.41 [0.06]	0.47 [0.03]	0.9	0.588	**F = 3.92** ***p* = 0.032**	**F = 10.7** ***p* = 7.5 × 10^{-3}**	F = 2.6 *p* = 0.13	F = 0.57 *p* = 0.46

Measurement	PHTS (*N* = 9) mean [SD]	NC (*N* = 9) mean [SD]	The rate of PHTS/NC	*R* squired	Corrected model	The presence of PHTS	Age	Gender
ILF, left	0.45 [0.05]	0.52 [0.02]	0.9	0.850	**F = 15.6** **$p = 1.7 \times 10^{-4}$**	**F = 40.3** **$p = 5.5 \times 10^{-5}$**	**F = 17.5** **$p = 0.0015$**	F = 0.051 $p = 0.82$
ILF, right	0.43 [0.08]	0.52 [0.02]	0.8	0.689	**F = 6.10** **$p = 7.7 \times 10^{-3}$**	**F = 16.3** **$p = 2.0 \times 10^{-3}$**	**F = 5.34** **$p = 0.041$**	F = 0.44 $p = 0.52$
IFOF, left	0.50 [0.05]	0.54 [0.03]	0.9	0.711	**F = 6.76** **$p = 5.3 \times 10^{-3}$**	**F = 10.0** **$p = 8.9 \times 10^{-3}$**	**F = 13.1** **$p = 0.004$**	F = 0.005 $p = 0.94$
IFOF, right	0.48 [0.04]	0.52 [0.03]	0.9	0.715	**F = 6.91** **$p = 4.9 \times 10^{-3}$**	**F = 12.3** **$p = 5.0 \times 10^{-3}$**	**F = 10.2** **$p = 8.4 \times 10^{-3}$**	F = 0.27 $p = 0.62$
UF, left	0.41 [0.06]	0.42 [0.02]	1.0	0.342	F = 1.43 $p = 0.29$	F = 1.07 $p = 0.32$	F = 0.47 $p = 0.51$	F = 1.75 $p = 0.21$
UF, right	0.43 [0.05]	0.43 [0.02]	1.0	0.502	F = 2.77 $p = 0.081$	F = 0.12 $p = 0.74$	F = 3.92 $p = 0.073$	F = 0.63 $p = 0.44$
CF, left	0.46 [0.06]	0.49 [0.04]	0.9	0.439	F = 2.15 $p = 0.14$	F = 1.12 $p = 0.31$	F = 1.42 $p = 0.26$	F = 2.26 $p = 0.16$
CF, right	0.46 [0.07]	0.46 [0.04]	1.0	0.649	**F = 5.1** **$p = 0.014$**	F = 0.082 $p = 0.78$	**F = 8.34** **$p = 0.015$**	F = 1.31 $p = 0.28$
FF, left	0.40 [0.08]	0.42 [0.04]	1.0	0.106	F = 0.33 $p = 0.85$	F = 0.12 $p = 0.74$	F = 0.04 $p = 0.85$	F = 0.30 $p = 0.59$
FF, right	0.37 [0.06]	0.40 [0.04]	0.9	0.188	F = 0.64 $p = 0.65$	F = 0.55 $p = 0.47$	F = 0.16 $p = 0.7$	F = 1.30 $p = 0.28$
CP	0.55 [0.04]	0.59 [0.03]	0.9	0.520	F = 2.98 $p = 0.068$	**F = 8.91** **$p = 0.012$**	F = 1.3 $p = 0.28$	F = 0.13 $p = 0.73$
ADC ($mm^2/s \times 10^{-5}$)								
AF, left	89.7 [8.1]	81.2 [3.7]	1.1	0.720	**F = 7.06** **$p = 4.5 \times 10^{-3}$**	**F = 13.1** **$p = 4.0 \times 10^{-3}$**	**F = 14.0** **$p = 3.2 \times 10^{-3}$**	F = 1.04 $p = 0.33$
AF, right	89.5 [7.8]	81.5 [4.0]	1.1	0.708	**F = 6.68** **$p = 5.6 \times 10^{-3}$**	**F = 14.2** **$p = 3.1 \times 10^{-3}$**	**F = 9.02** **$p = 0.012$**	F = 0.17 $p = 0.69$
ILF, left	97.9 [5.6]	88.8 [3.7]	1.1	0.706	**F = 6.59** **$p = 5.9 \times 10^{-3}$**	**F = 19.5** **$p = 0.001$**	**F = 6.32** **$p = 0.029$**	F = 0.19 $p = 0.67$
ILF, right	97.6 [10.8]	90.5 [2.4]	1.1	0.477	F = 2.51 $p = 0.10$	F = 2.51 $p = 0.14$	**F = 7.15** **$p = 0.022$**	F = 1.11 $p = 0.31$

Measurement	PHTS (*N* = 9) mean [SD]	NC (*N* = 9) mean [SD]	The rate of PHTS/NC	*R* squired	Corrected model	The presence of PHTS	Age	Gender
IFOF, left	93.2 [5.6]	85.3 [3.7]	1.1	0.750	**F = 8.25** ***p* = 2.5 × 10^{-3}**	**F = 27.8** ***p* = 2.6 × 10^{-4}**	F = 3.29 *p* = 0.097	F = 0.65 *p* = 0.44
IFOF, right	90.7 [8.4]	86.5 [3.5]	1.1	0.388	F = 1.75 *p* = 0.21	F = 2.67 *p* = 0.13	F = 3.98 *p* = 0.07	F = 0.20 *p* = 0.66
UF, left	92.2 [6.5]	87.8 [3.1]	1.1	0.440	F = 2.16 *p* = 0.14	**F = 5.41** ***p* = 0.04**	F = 2.07 *p* = 0.18	F = 0.20 *p* = 0.66
UF, right	89.3 [5.8]	88.1 [2.6]	1.0	0.475	F = 2.49 *p* = 0.10	F = 0.70 *p* = 0.42	**F = 6.51** ***p* = 0.027**	F < 1.0 × 10^{-4} *p* = 1.0
CF, left	91.6 [10.8]	84.7 [3.4]	1.1	0.228	F = 0.81 *p* = 0.54	F = 2.35 *p* = 0.15	F = 0.53 *p* = 0.48	F = 7.2 × 10^{-3} *p* = 0.93
CF, right	88.2 [8.4]	85.2 [2.8]	1.0	0.539	**F = 3.22** *p* = 0.056	F = 2.90 *p* = 0.12	**F = 5.4** ***p* = 0.04**	F = 0.34 *p* = 0.57
FF, left	119.7 [23.6]	120.8 [13.5]	1.0	0.090	F = 0.27 *p* = 0.89	F = 0.12 *p* = 0.74	F = 0.26 *p* = 0.62	F = 0.62 *p* = 0.45
FF, right	123.8 [18.1]	127.6 [14.9]	1.0	0.179	F = 0.60 *p* = 0.67	F = 0.095 *p* = 0.76	F = 0.29 *p* = 0.6	F = 0.016 *p* = 0.90
CP	91.2 [6.6]	88.0 [3.6]	1.0	0.537	**F = 3.19** *p* = 0.057	**F = 5.88** ***p* = 0.034**	F = 3.53 *p* = 0.087	F = 0.043 *p* = 0.84

Abbreviations: ADC, apparent diffusion coefficient; AF, arcuate fasciculus; CF, cingulum fasciculus; CP, callosal pathway; DTI, Diffusion tensor imaging; FA, fractional anisotropy; FF, fornix fasciculus; IFOF, inferior fronto-occipital fasciculus; ILF, inferior longitudinal fasciculus; NC, Neurotypical controls; PHTS, *PTEN* hamartoma tumor syndrome; SD, Standard deviation; UF, uncinate fasciculus.

Bold entries indicate a measurement exhibiting statistically significant group-wise differences. A General Linear Model ($p < 0.05$) was constructed to evaluate the effects of continuous or binary covariates (age and gender). Critical values from the *F*-distribution calculation were determined to be $F(0.05,4,13) = 3.18$ and $F(0.05,1,13) = 4.67$, for the corrected model and each covariate, respectively.